



HAL
open science

Magnetized Winds of M-type Stars and Star–Planet Magnetic Interactions: Uncertainties and Modeling Strategy

Victor Réville, Jamie M. Jasinski, Marco Velli, Antoine Strugarek, Allan Sacha Brun, Neil Murphy, Leonardo H. Regoli, Alexis P. Rouillard, Jacobo Varela

► **To cite this version:**

Victor Réville, Jamie M. Jasinski, Marco Velli, Antoine Strugarek, Allan Sacha Brun, et al.. Magnetized Winds of M-type Stars and Star–Planet Magnetic Interactions: Uncertainties and Modeling Strategy. *The Astrophysical Journal*, 2024, 976, 10.3847/1538-4357/ad8132 . insu-04833926

HAL Id: insu-04833926

<https://insu.hal.science/insu-04833926v1>

Submitted on 12 Dec 2024

HAL is a multi-disciplinary open access archive for the deposit and dissemination of scientific research documents, whether they are published or not. The documents may come from teaching and research institutions in France or abroad, or from public or private research centers.

L'archive ouverte pluridisciplinaire **HAL**, est destinée au dépôt et à la diffusion de documents scientifiques de niveau recherche, publiés ou non, émanant des établissements d'enseignement et de recherche français ou étrangers, des laboratoires publics ou privés.



Distributed under a Creative Commons Attribution 4.0 International License



Magnetized Winds of M-type Stars and Star–Planet Magnetic Interactions: Uncertainties and Modeling Strategy

Victor Réville¹ , Jamie M. Jasinski² , Marco Velli² , Antoine Strugarek³ , Allan Sacha Brun³ , Neil Murphy² ,
Leonardo H. Regoli⁴ , Alexis P. Rouillard¹ , and Jacobo Varela⁵

¹IRAP, Université Toulouse III—Paul Sabatier, CNRS, CNES, Toulouse, France

²NASA Jet Propulsion Laboratory, California Institute of Technology, Pasadena, CA 91011, USA

³Département d’Astrophysique/AIM, CEA/IRFU, CNRS/INSU, Univ. Paris-Saclay & Univ. de Paris, 91191 Gif-sur-Yvette, France

⁴Johns Hopkins Applied Physics Laboratory, Laurel, MD 20723, USA

⁵Institute for Fusion Studies, Department of Physics, University of Texas at Austin, Austin, TX 78712, USA

Received 2024 August 7; revised 2024 September 26; accepted 2024 September 26; published 2024 November 13

Abstract

M-type stars are the most common stars in the Universe. They are ideal hosts for the search of exoplanets in the habitable zone (HZ), as their small size and low temperature make the HZ much closer-in than their solar twins. Harboring very deep convective layers, they also usually exhibit very intense magnetic fields. Understanding their environment, in particular their coronal and wind properties, is thus very important, as they might be very different from what is observed in the solar system. The mass-loss rate of M-type stars is poorly known observationally, and recent attempts to estimate it for some of them (e.g., TRAPPIST-1 and Proxima Centauri) can vary by an order of magnitude. In this work, we revisit the stellar wind properties of M dwarfs in the light of the latest estimates of \dot{M} through Ly α absorption at the astropause and slingshot prominences. We outline a modeling strategy to estimate the mass-loss rate, radiative loss, and wind speed, with uncertainties, based on an Alfvén-wave-driven stellar wind model. We find that it is very likely that several TRAPPIST-1 planets lie within the Alfvén surface, which implies that these planets experience star–planet magnetic interactions (SPMIs). We also find that SPMIs between Proxima Cen b and its host star could be the reason for recently observed radio emissions.

Unified Astronomy Thesaurus concepts: [Stellar winds \(1636\)](#); [M stars \(985\)](#); [Exoplanets \(498\)](#); [Magnetohydrodynamics \(1964\)](#)

1. Introduction

The characterization of cool M-dwarf astrospheres is of primary importance to the study of the environment of their orbiting planetary systems. M-dwarf stars are very active, creating large average magnetic fields in their deep convective envelope, up to the kilogauss scale (A. Reiners & G. Basri 2010; C. Moutou et al. 2017; A. Reiners et al. 2022). Even slow rotators have been recently shown to be able to create a few hundred gauss fields, largely above the expected strength from their Rossby number (L. T. Lehmann et al. 2024). The correlation between the field strength and coronal heating of solar-like stars is moreover well established (see, e.g., M. Güdel 2004), which directly translates into more wind power for higher stellar magnetic fields. The indirect observations of stellar winds using the Ly α absorption signatures of the astrospheres (B. E. Wood et al. 2005) provides a power law relating the X-ray power of the corona and the mass-loss rate of cool stars. This relation has been reassessed recently using new measurements of M-dwarf and slingshot prominences detected in very active stars (M. Jardine & A. Collier Cameron 2019; B. E. Wood et al. 2021).

The mass-loss rate is however the only true constraint that we possess on the properties of distant stellar winds. Many parameters that are relevant to the interaction of exoplanets with the stellar environment are not observable remotely. For example, knowing the mass-loss rate and the stellar wind speed provides the dynamic pressure, but the wind speed is unknown for all main-

sequence stars but the Sun. The dynamic pressure is essential to compute the magnetospheric stand-off distance, in addition to knowing the planetary magnetic field (see, e.g., J. Varela et al. 2022a, 2022b). Moreover extreme-ultraviolet (EUV) emissions are difficult to constrain, being mostly absorbed in the interstellar medium. Yet, the EUV flux is among the main factors impacting the atmospheric escape rate of exoplanets (A. Lecavelier Des Etangs 2007; V. Bourrier et al. 2017a).

In the particular context of M dwarfs, for which potentially habitable planets lie very close to the star, another interesting question arises. Given their very intense magnetic fields, one can wonder whether planets in the habitable zone (HZ) also orbit within the Alfvén surface of the star, i.e., at a distance where the planet can have a magnetic influence on its host. Star–planet magnetic interactions (SPMIs; see A. Strugarek et al. 2015, 2019) can influence the secular orbital evolution of systems (A. Strugarek et al. 2014), and are expected to generate intense energy exchange between the planet and the star (A. Strugarek et al. 2022).

Recently, strong radio emission coming from Proxima Centauri (hereafter Proxima Cen) have been detected (M. Pérez-Torres et al. 2021). With a semimajor axis of $\sim 74R_{\odot}$ (G. Anglada-Escudé et al. 2016), Proxima Cen b has been proposed as a possible source of these radio emissions, through a cyclotron maser emission process analogous to the Io–Jupiter interaction (P. Zarka et al. 1996). Previous simulations of the Proxima Cen system have claimed that planet b should lie outside the Alfvén surface (C. Garraffo et al. 2016; R. D. Kavanagh et al. 2021). While both based on the Alfvén-wave-driven solar wind model AwSoM (B. van der Holst et al. 2014), they use various magnetic field constraints on the inner boundary and obtain very different mass-loss rates, very well above the nondetection limit of B. E. Wood et al. (2001) in the

case of C. Garraffo et al. (2016). The same kind of discrepancies are found within studies of the TRAPPIST-1 system, in which seven close-in planets have been discovered (M. Gillon et al. 2016, 2017). For this particular system, the predictions made with the AwSoM code have either most of the orbiting planets within the Alfvén surface (C. Garraffo et al. 2017), or none (C. Dong et al. 2018). The resulting mass-loss rates are also very different, varying between $1\dot{M}_\odot$ (C. Garraffo et al. 2017) and $0.1\dot{M}_\odot$ (C. Dong et al. 2018), which likely explains part of these differences.

In this work, we propose to reevaluate the stellar wind modeling strategy guided by the updated measurements of B. E. Wood et al. (2021). We perform nine simulations using the Alfvén-wave-driven solar wind model WindPredict-AW, varying the main input parameters. In Section 2, we discuss briefly the observed mass-loss rate constraints. Section 3 describes the fundamentals of the WindPredict-AW model, and the modifications brought to the code for the case of M dwarfs. Then, Section 4 shows the results of the simulations and the various channels into which the input energy is distributed: radiation, mass loss, and wind acceleration. We show that the characteristics of the turbulence play a key role in the terminal wind speed. We highlight the stellar wind conditions that should be characteristic of the TRAPPIST-1 system, and find, in Section 5, that inner TRAPPIST-1 planets should orbit within the Alfvén surface, giving birth to SPMIs. We also reassess the situation of Proxima Cen b, and find that it could well be the source of strong radio emissions. Finally, in Section 6, we explore ways to assess the X-ray and UV spectra of M dwarfs, and use them to constrain our simulations.

2. Mass-loss Rate Observations

The B. E. Wood et al. (2021) $F_X - \dot{M}$ relationship can be expressed as follows:

$$\frac{\dot{M}_\star}{R_\star^2} = \frac{\dot{M}_\odot}{R_\odot^2} \left(\frac{F_{X,\star}}{F_{X,\odot}} \right)^{0.77 \pm 0.04}, \quad (1)$$

where F_X is the X-ray flux, and \dot{M} the mass-loss rate. Figure 1 shows the 35 measured mass-loss rates through the astrospheric detection method (B. E. Wood et al. 2005) and the slingshot prominence technique (M. Jardine & A. Collier Cameron 2019). The Sun is added with a \odot symbol, while M-dwarf and subgiant/giant stars are identified with red stars and blue diamonds, respectively. Main-sequence G-K stars are represented with green dots. In this plot, we chose a solar X-ray flux $F_{X,\odot} = 10^{27.3} \text{ erg s}^{-1}$, and a mass-loss rate of $\dot{M}_\odot = 1.5 \times 10^{12} \text{ g s}^{-1}$, which is slightly higher than the value used in B. E. Wood et al. (2021), and consistent with the activity maximum (P. G. Judge et al. 2003).

The blue line (Equation (1)) shows the uncertainties in the exponent, represented in blue shades. One can see, however, that the spread remains much larger than these uncertainties, and we added two curves multiplying by a factor 0.1 and 10 the fitted law, shown in dashed blue color. These two curves do cover most of the data points, except for two points in the lowest part of the diagram, corresponding to the giants stars λ And and DK UMA (see B. E. Wood et al. 2021, for more details).

In the following, we will aim to model the wind of two specific M dwarfs, TRAPPIST-1 and Proxima Cen, with mass-loss rates compatible with this observationally constrained scaling law.

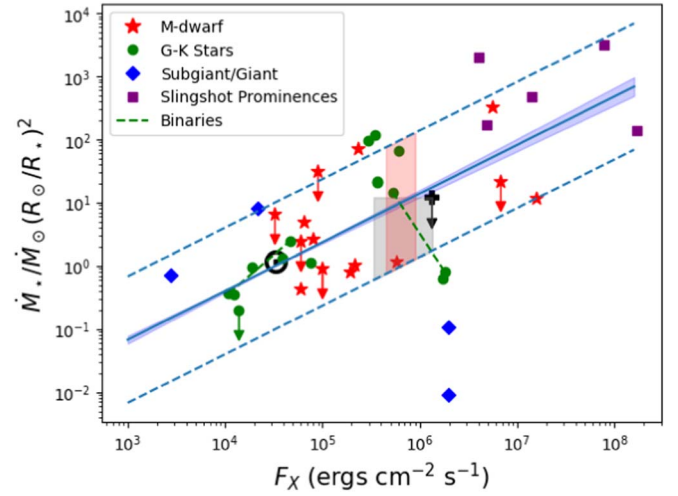


Figure 1. The B. E. Wood et al. (2021) $\dot{M} - F_X$ law with updated measurements from M dwarfs and slingshot prominences. The blue line represents the fitted law (Equation (1)). The dashed lines, one-tenth and 10 times the fitted law, encompass most of the 36 data points, with only a few outliers on the subgiant/giant branch. The filled regions in red and gray correspond to the mass-loss rate estimates for TRAPPIST-1 and Proxima Cen, respectively. The black cross symbol is the upper bound for Proxima Cen (all down arrows represent upper bounds).

Given the uncertainties illustrated in Figure 1, we shall consider that a mass-loss rate of 1 order of magnitude lower or higher than the one predicted by Wood’s law is perfectly plausible. The range of expected mass-loss rates is highlighted in gray shades for Proxima Cen given the quiet X-ray luminosity $L_X = 4\text{--}16 \times 10^{26} \text{ erg s}^{-1}$ (B. M. Haisch et al. 1990). It is bounded by the nondetection limit found by B. E. Wood et al. (2001) and shown with the black cross. The equivalent mass-loss rate range is shown in red shades for TRAPPIST-1, for measured $L_X = 4\text{--}8 \times 10^{26} \text{ erg s}^{-1}$ (P. J. Wheatley et al. 2017).

3. Numerical Model

We use the WindPredict-AW model (V. Réville et al. 2020; S. Parenti et al. 2022), based on the PLUTO code (A. Mignone et al. 2007). The implementation is very similar to the one described in V. Réville et al. (2021, 2022), where we use a chromospheric boundary condition with a transition region (TR). The boundary conditions are extensively discussed in S. Parenti et al. (2022), the only difference being that the temperature is held fixed at the chromospheric inner boundary.

The model solves the ideal MHD equations, assuming that the wind driving is solely due to the turbulent heating and wave pressure of Alfvén-wave packets propagating from the surface of the Sun. We neglect any heating contribution from impulsive events such as nanoflares (E. N. Parker 1988) that would require resistivity. The ideal MHD system is thus complemented by two equations for Alfvén-wave transport and dissipation. These equations read

$$\begin{aligned} \frac{\partial \mathcal{E}^\pm}{\partial t} + \nabla \cdot ([\mathbf{v} \pm \mathbf{v}_A] \mathcal{E}^\pm) \\ = - \frac{\mathcal{E}^\pm}{2} \nabla \cdot \mathbf{v} - (\mathcal{R}^\pm \mathcal{E}^\pm - \mathcal{R}^\mp \mathcal{E}^\mp) - Q_w^\pm, \end{aligned} \quad (2)$$

where $\mathcal{E}^\pm = \rho|z^\pm|^2/4$ is the energy density of the Alfvén-wave packets, defined by the Elsässer variables:

$$z^\pm = \delta v \mp \text{sign}(B_r) \frac{\delta b}{\sqrt{4\pi\rho}}. \quad (3)$$

The turbulence dissipation term is defined as

$$Q_w^\pm = \frac{\rho}{8} \frac{|z^\pm|^2}{\lambda} |z^\mp|, \quad (4)$$

where $\lambda = \lambda_* \sqrt{\langle B_* \rangle / |B|}$ is the turbulence correlation length scale, and \mathcal{R}^\pm is the reflection coefficient of Alfvén waves in the expanding solar wind, and is defined as

$$\mathcal{R}^\pm = |V_{A,r} \nabla_r \sqrt{\ln \rho}| \times \text{MAX}\left(0, 1 - \frac{\mathcal{E}^\mp}{\mathcal{E}^\pm}\right). \quad (5)$$

This represents the main modification compared to previous versions of WindPredict-AW. The form of the reflection term is inspired by the incompressible equations for Alfvén waves (see, e.g., M. Velli 1993), and is very close to similar models (B. van der Holst et al. 2014; C. Shi et al. 2023). This term makes the reflection proportional to the density (or Alfvén speed) gradients in the solar wind. Around the TR, the inverse reflection timescale $|V_{A,r} \nabla_r \sqrt{\ln \rho}|$ is however very large due to the magnetic field amplitude, and thus it is limited by the ratio of the two Elsässer populations, up to a roughly balanced turbulence ($|z^+| \sim |z^-|$). The max term also guarantees that only the dominant wave population undergoes reflection, which ensures a global conservation of energy in the system: The reflection loss and gain term compensates exactly, while the dissipation term is converted into heat by the energy conservation equation.

The energy sources and sinks are $Q = Q_w - Q_r - Q_c$, the sum of the wave energy dissipation $Q_w = Q_w^+ + Q_w^-$ and the radiative losses $Q_r = n^2 \Lambda(T)$, where Λ is computed as a fit to the CHIANTI database radiative loss function for solar coronal abundances (version 10.0.1, K. P. Dere et al. 1997; J. T. Schmelz et al. 2012; G. Del Zanna et al. 2021).

A few modifications have been made to the thermal conduction sink term Q_c , in order to account for much larger closed loops compared to the solar case. It is implemented as

$$Q_c = \nabla \cdot (\alpha \mathbf{q}_s + (1 - \alpha) \mathbf{q}_p), \quad (6)$$

where $\alpha = 1/(1 + (r - R_\odot)^2/(r_{\text{coll}} - R_\odot)^2)$. We changed here the radial dependence of the parameter α from a power-law decrease of index -4 to -2 . The height at which the transition between the collisional and collisionless regimes remains $r_{\text{coll}} = 5R_\odot$, but the parabolic Braginskii thermal diffusion, $\mathbf{q}_s = -\kappa_0 T^{5/2} (\hat{\mathbf{b}} \cdot \nabla T) \hat{\mathbf{b}}$, is still significant up to $20R_\odot$. We then set the collisionless electron heat flux $\mathbf{q}_p = 4p_{\text{th}} (\hat{\mathbf{b}} \cdot \mathbf{v}) \hat{\mathbf{b}}$, for which the prefactor has been raised from $3/2$ to 4 compared to previous papers, in agreement with the analytical calculations of J. V. Hollweg (1976).

The base density and temperature are set to $n_* = 2 \times 10^{13} \text{ cm}^{-3}$ and $T_* = 3000 \text{ K}$. The base density is about 10 times higher than for similar typical solar wind simulations, while the temperature is the characteristic photospheric temperature for M dwarfs. The stellar atmosphere hence goes through a TR where the temperature jumps up to a few 10^6 K . We use a 2.5D spherical grid with [896, 256] points to cover the domain $r \in [1, 130R_*]$ and $\theta \in [0, \pi]$. The grid is strongly refined at the

Table 1
Observational Parameters of TRAPPIST-1

Qty	Value	References
R_*	$0.121R_\odot$	V. Van Grootel et al. (2018)
M_*	$0.089M_\odot$	V. Van Grootel et al. (2018)
Bf	600 G	A. Reiners & G. Basri (2010)
P_{rot}	3.3 days	R. Luger et al. (2017)
F_X	$4-8 \times 10^{26} \text{ erg s}^{-1}$	P. J. Wheatley et al. (2017)

inner boundary, as well as near the temperature maximum between 1 and $4R_*$. Moreover, some numerical adjustments are necessary to properly describe the energy transfer in the TR. For this, we use the technique of R. Lionello et al. (2009), which sets a cutoff temperature under which the product of the thermal conduction and the radiative losses is kept constant. We set the cutoff temperature to $T_c = 4 \times 10^5 \text{ K}$. This comes down to multiplying the terms Q_r and Q_w by a factor $T^{5/2}/T_c^{5/2}$, which ensures that the integrated energy terms are the same as with a fully resolved TR (see C. D. Johnston et al. 2020, for more details). This will be very important for the following analysis, as shown in Sections 4 and 6.

The remaining input parameters are thus the initial and inner boundary magnetic fields, the transverse velocity perturbation δv_* , and the turbulence correlation length λ_* at the base of the domain. In the next section, we will vary the two latter parameters to model the wind of one specific M-dwarf system: TRAPPIST-1.

4. Application to the TRAPPIST-1 System

4.1. Simulation Results

Observational constraints of the TRAPPIST-1 system are summarized in Table 1. The radius and mass of the host star set the rest of the normalization triplet (n_* , R_* , V_*), the normalization length R_* , and velocity $v_{\text{kep},*} = \sqrt{GM_*/R_*}$. A. Reiners & G. Basri (2010) measured the magnetic flux of TRAPPIST-1 through Zeeman broadening $Bf = 600 \text{ G}$, where f is the magnetic filling factor. Without any Zeeman Doppler inversion (J. F. Donati & C. Moutou, 2024, private communication), we are not able to recover the energy partition of the magnetic field decomposed on spherical harmonics, and we thus assume a simple dipole with $\langle B_r \rangle = 600 \text{ G}$. This is reasonable as observed M-dwarf magnetic fields do show a strong dipolar component (see, e.g., J. Morin et al. 2008; L. T. Lehmann et al. 2024). Moreover, even though more complex field can lead to smaller Alfvén surfaces (V. Réville et al. 2015), the dipole component is what sets the properties of the wind to zeroth order (A. J. Finley & S. P. Matt 2017, 2018). These observed dipoles are however not generally aligned with the stellar rotation axis, which leads to time-dependent structure of the magnetic sectors. These aspects are out of the scope of the present paper. Moreover, given the weak surface rotation velocity of TRAPPIST-1 and Proxima Cen, we do not expect rotation to have a strong influence on the final solution (such as magneto-centrifugal effects; see V. Réville et al. 2015), and we thus consider that our 2.5D simulation can represent any inclination angle with respect to the ecliptic plane. The rotation period is accounted for in the rotating frame, with a rotation velocity at the stellar surface $v_{\text{rot}}/v_{\text{esc}} = 3.5 \times 10^{-3}$ for TRAPPIST-1.

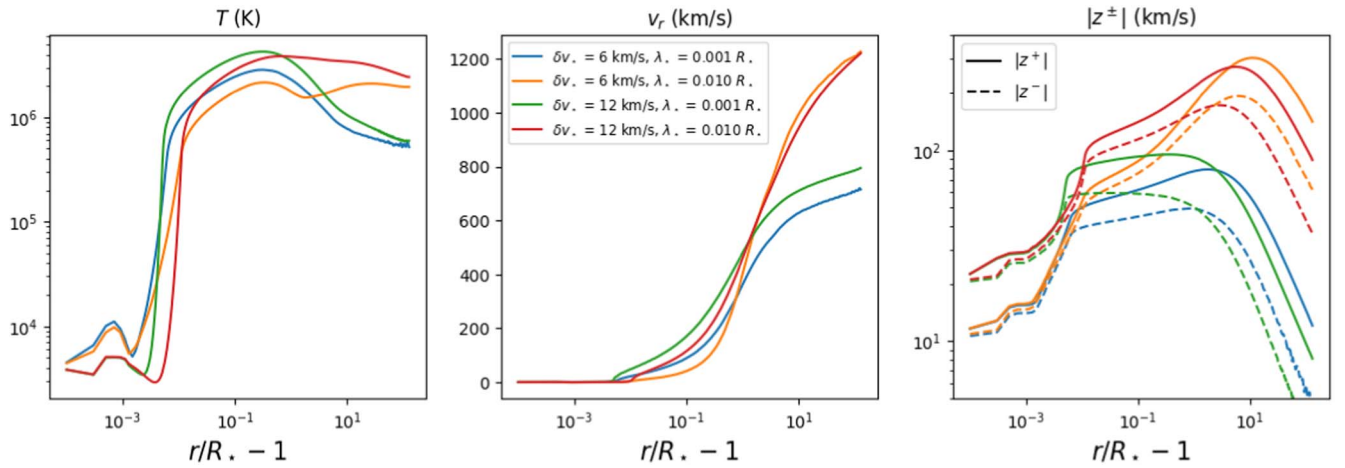


Figure 2. Profiles of the coronal temperature, radial wind speed, and wave populations along open field regions for four simulations.

Table 2
Simulation Parameters and Results

δv_* (km s^{-1})	λ_* (R_*)	L_p (erg s^{-1})	\dot{M}/\dot{M}_\odot	$\langle R_{A,j} \rangle / R_*$
3	0.001	1.28e28	0.085	85
6	0.001	6.36e28	0.64	52
12	0.001	2.82e29	4.4	36
24	0.001	1.24e30	31.9	22
3	0.01
6	0.01	5.36e28	0.25	66
12	0.01	2.41e29	1.79	45
24	0.01	1.13e30	13.6	29

With the boundary magnetic field set, we now vary the input wave forcing δv_* and the turbulence correlation length scale λ_* . We perform eight simulations with an increasing value of δv_* and two values for the turbulence correlation scale. Table 2 summarizes the parameters and results of the eight simulations. Note that for $\delta v_* = 3 \text{ km s}^{-1}$ and $\lambda_* = 0.01 R_*$, the code was not able to maintain high-temperature regimes in the coronal domain. Tests suggest that further numerical developments are required to reach a physically meaningful steady state for this set of parameters.

Figure 2 shows profiles of the temperature, radial wind speed, and Alfvén-wave amplitudes for a subset of four simulations, with $\delta v_* = 6, 12 \text{ km s}^{-1}$, and $\lambda_* = 0.01, 0.001 R_*$. The temperature of the stellar wind goes from 3000 K up to 1–4 MK depending on the simulation parameters. The maximum temperature is logically a growing function of the input δv_* . One can notice also that high temperatures are sustained much further away from the star for $\lambda_* = 0.01 R_*$. This can be understood looking at the profiles of the Elsässer amplitudes. While starting with similar values, both wave species are dissipated lower in the corona for the highest value of λ_* . As a result, their amplitudes remain much below 100 km s^{-1} , while they can reach 300 km s^{-1} for $\lambda_* = 0.01 R_*$. This generally also explains the velocity profiles, which are strongly dependent on the value of λ_* . The fastest winds are obtained for low values of λ_* , because of the ponderomotive force (or wave pressure), which acts as an external momentum source for the wind speed. The stellar “fast” wind components thus range between ~ 700 and $\sim 1200 \text{ km s}^{-1}$, which is much higher than the fast solar wind.

Finally, the left panel of Figure 2 shows that in the chromosphere the turbulence is almost balanced, i.e., $|z^+| \sim |z^-|$, due to the strong reflection below the TR (see Equation (5)). Consequently, part of the wave energy injected at the boundary in the outgoing wave reenters the domain with the oppositely propagating wave population. We use an outflow boundary condition for the inward-propagating wave at the inner boundary, and the effective energy injected is thus a result of the simulation. In Table 2, we report the effective input Poynting luminosity (see Section 4.2) resulting from this boundary condition.

The four panels of Figure 3 show 2D views of each simulation, the radial wind speed, the logarithm of the temperature, the radial Alfvén speed, and the velocity perturbations. The global structure of each simulation is very reminiscent of typical solar wind simulations, with open solar wind structures at the two poles of the dipole and closed loops followed by a current sheet and plasma sheet around the equator. The wind speed is modulated by the magnetic structure, with higher wind speeds coming from coronal holes and lower wind speeds around the current sheet.

Closed coronal loops, or helmet streamers, are nonetheless much larger than any solar structure, especially for cases with low δv_* . In the case with $\delta v_* = 6 \text{ km s}^{-1}$, the tip of these streamers goes beyond $20 R_*$, which necessitated some changes in our numerical techniques (see Section 3). From the first column, we can observe that the fastest wind speed is between 600 and 800 km s^{-1} for the three simulations with $\lambda_* = 0.001 R_*$, while it reaches 1200 km s^{-1} for $\lambda_* = 0.01 R_*$.

We plot in Figure 4 the characteristic slow and fast wind speeds and the subsequent range of possible wind speeds for each set of simulations. We computed the area-weighted average speed of each wind component at a distance of $100 R_*$, where we assume that the terminal velocity is reached. This plot shows even more clearly the strong dependency of the wind speed on λ_* . The wind speed is a growing function of λ_* and, in most cases, also a growing function of δv_* (see Figure 4). Nevertheless, we observe a nonmonotonic behavior of the wind speed at low δv_* . This is a reminder that the dynamics of Alfvén-wave turbulent transport is nontrivial. In essence, because of the lower heating for $\delta v_* = 3 \text{ km s}^{-1}$, the wind is very tenuous, which in return yields higher Alfvén speeds and stronger amplification of Alfvén waves in the corona, which is able to accelerate the wind to higher velocities.

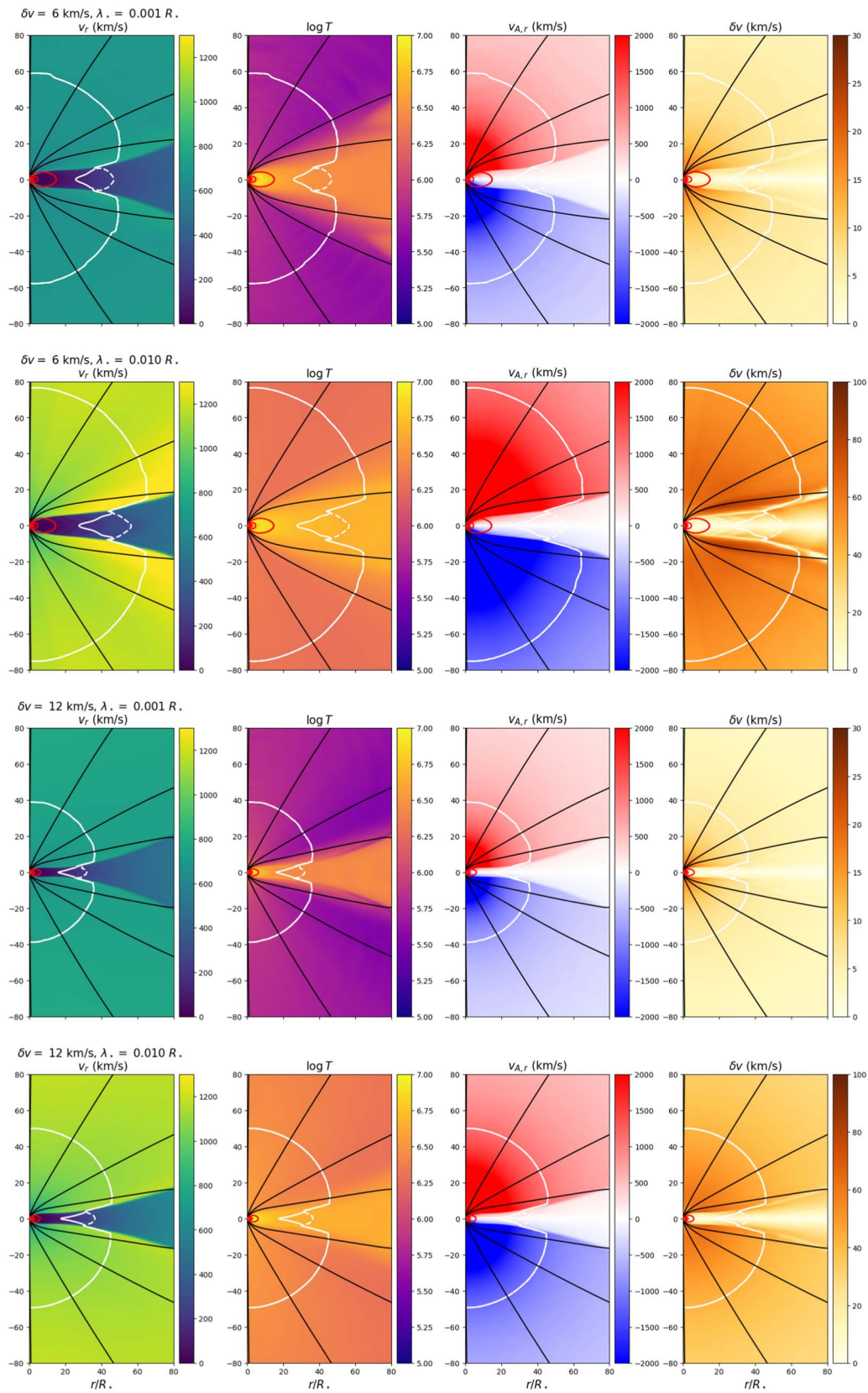


Figure 3. Summary of four cases with the radial velocity, logarithm of temperature, radial Alfvén speed ($B_r/\sqrt{4\pi\rho}$), and velocity perturbation δv . The (fast) Alfvén surface is shown in (dashed) white on top of each panel, while open (closed) magnetic field lines are shown in black (red). The δv color scale varies for cases with different λ_* .

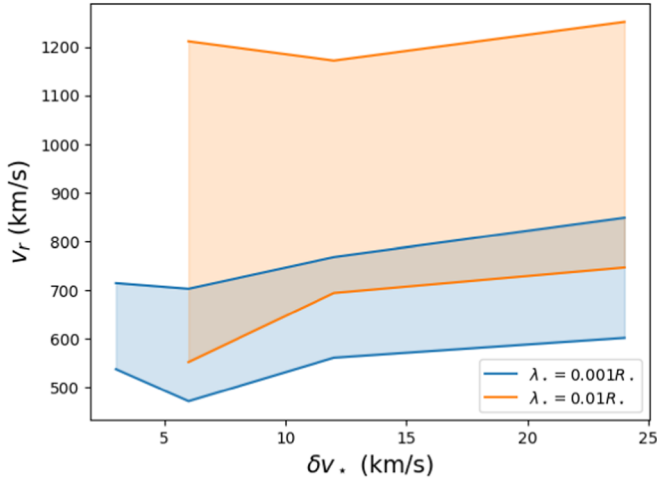


Figure 4. Fast and slow wind speeds as a function of δv_* and values of λ_* . The fast wind speed increases strongly with increasing value of λ_* , reaching some 1200 km s^{-1} for $\lambda_* = 0.01$, with a much weaker dependence on δv_* .

In the solar corona, close to the surface, closed regions and sources of slow wind are hotter than open field areas, due to higher expansion rates that increase heating. This trend reverses further away, where the fast wind becomes hotter than the slow wind (see S. Hazra et al. 2021, for simulations of the solar cycle). For the TRAPPIST-1 system, we also observe hotter slow wind close-in, but the slow wind remains hotter than the fast wind throughout the simulation domain. It is nonetheless likely that this transition is only displaced further away due to the very intense magnetic field of M dwarfs. There is also a greater contrast in the temperatures between the slow and fast winds depending on the value of λ_* . We recover the property seen in Figure 2, that megakelvin temperatures are sustained to further distances with higher λ_* . This can be understood rather straightforwardly. The turbulence correlation length scale parameter controls the scale height of turbulent heating in the stellar wind, and lower values will tend to concentrate the heating in the chromosphere and very low corona. This will not only load the stellar wind to higher densities but also dissipate Alfvén waves much more efficiently close to the star. As such, as shown in the leftmost panels of Figures 2 and 3, there is much less wave energy to heat the solar corona at a further distance from the star.

4.2. Energetics

Let us now discuss the global energetics of the simulations. Assuming steady state, the energy equation can be written as

$$\nabla \cdot \mathbf{F}_E = \nabla \cdot \left[\rho \mathbf{v} \left(\frac{1}{2} v^2 + \frac{c_s^2}{\gamma - 1} - \frac{GM_*}{r} \right) + \mathbf{F}_p + \mathbf{F}_c \right] = -Q_r, \quad (7)$$

where \mathbf{F}_E is the total energy flux, \mathbf{F}_p the Poynting flux, and \mathbf{F}_c the conduction flux. Integrating this equation between the surface S_* and a spherical surface S_∞ at great distance from the star R_∞ , we have

$$\int_{S_\infty} \mathbf{F}_E \cdot d\mathbf{S} + \int_{R_*}^{R_\infty} Q_r dV = \int_{S_*} \mathbf{F}_E \cdot d\mathbf{S}. \quad (8)$$

At the photosphere, the wind speed and sound speed are very small compared to the gravity potential, and the dominant

terms of \mathbf{F}_E are the Poynting flux \mathbf{F}_p and the gravity term. Far away from the star, only the kinetic energy term remains, so that we are left with

$$\int_{S_\infty} \left(\frac{1}{2} v^2 \right) \rho \mathbf{v} \cdot d\mathbf{S} + \int_{R_*}^{R_\infty} Q_r dV = \int_{S_*} (\mathbf{F}_p - \rho \mathbf{v} \frac{GM_*}{r}) \cdot d\mathbf{S}. \quad (9)$$

Using mass conservation and $GM_*/R_* = v_{\text{esc}}^2/2$, we can write this equation in terms of \dot{M} :

$$\dot{M} (v_{\text{esc}}^2 + v_\infty^2)/2 + \int_{R_*}^{R_\infty} Q_r dV = \int_{S_*} \mathbf{F}_p \cdot d\mathbf{S}, \quad (10)$$

so that we finally can rewrite in terms of luminosity:

$$L_K \left(1 + \frac{v_{\text{esc}}^2}{v_\infty^2} \right) + L_{\text{rad}} = L_p, \quad (11)$$

with $L_K = \dot{M} v_\infty^2/2$, while the other terms are defined by the integrals of Equation (10).

Figure 5 illustrates this latter equation. Logically, the blue radiative and red kinetic terms are growing functions of the input Poynting flux. The kinetic term is a power law of the input Poynting flux with a slope of roughly 1.4. Note that this dependence differs from the exponential dependence found in S. Hazra et al. (2021). The reason is that we now include the TR with a fixed low chromospheric temperature, which has a negligible influence on the energy budget and the mass-loss rate (see also M. Velli 2010). The radiative losses largely dominate the energetic balance, and thus grow almost linearly with the input Poynting luminosity. This is due in large part to the closed regions of the simulations, where in steady state radiative losses match the input energy at the coronal loop footpoints. But a significant part of the input energy is also lost in radiation in open regions. The sum of the radiative and twice the kinetic terms is close, as expected, to the total input energy illustrated with the $y = x$ line (assuming that $v_\infty \sim v_{\text{esc}}$, Equation (11) becomes $2L_K + L_{\text{rad}} = L_p$). The differences are likely due to numerical integration of these terms on the first domain cells during post-processing, as the radiative losses can be very significant in these regions.

The horizontal black line shows the expected kinetic luminosity using the B. E. Wood et al. (2021) law. We used the target mass-loss rate of $\dot{M} = 2.25 \times 10^{11} \text{ g s}^{-1}$, and a terminal velocity $v_\infty = 900 \text{ km s}^{-1}$, consistent with the values obtained in our simulations. As we can see, the simulations with the smallest $\delta v_* = 3, 6 \text{ km s}^{-1}$ are within the range of uncertainties for Wood's law shown in red shades (same as Figure 1). Moreover, simulations with $\delta v_* = 12 \text{ km s}^{-1}$ are right at the upper bound of this region. We can thus reasonably assume that this ensemble of simulations is representative of the TRAPPIST-1 system.

Figure 5 finally shows that the global energetics vary little with the turbulence correlation scale, in agreement with Equation (10). However, as discussed at length in the previous section and as shown in Figures 2 and 3, the terminal wind speed can vary significantly, more than 2 times the escape velocity of 529 km s^{-1} , for the highest value of the turbulence correlation length scale.

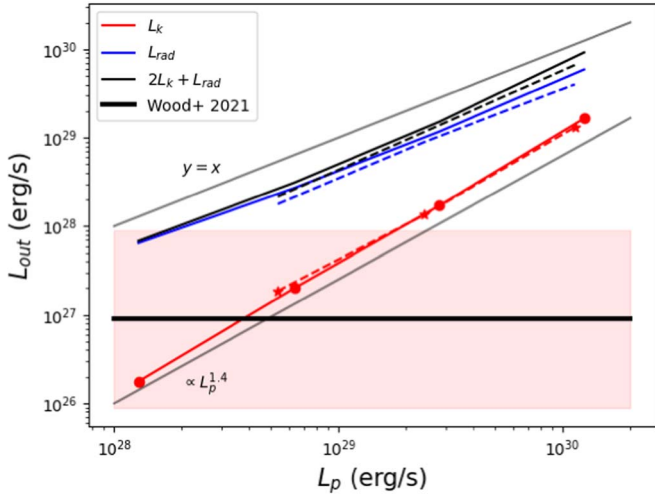


Figure 5. Illustration of the energy balance in our simulations according to Equations (10)–(11). Red lines correspond to the kinetic energy luminosity while dark blue lines correspond to the radiated energy. The sum is shown in black and corresponds to the expected input energy in light blue. Dashed lines are used when the turbulence correlation length scale $\lambda_* = 0.01$. The target mass-loss rate (expressed in kinetic luminosity) is given by the horizontal dark line, with the reported uncertainties of Figure 1 in red shades.

5. Alfvén Surface and Potential Star–Planet Interactions

5.1. The TRAPPIST-1 System

Figure 3 shows in white contours the structure of the Alfvén surface in each of the runs. These surfaces have the shape typical of dipolar winds, with two lobes above the poles harboring the largest values of the Alfvén radius and lower values around the equator. There the Alfvén surface joins the tip of the largest steady closed loop, between $20R_*$ and $30R_*$.

Furthermore, for star–planet magnetic interactions to exist, having the planet lie within the fast magneto-acoustic surface of the stellar wind suffices. In practice, due to the relatively low rotation of the TRAPPIST-1 planet (the breakup ratio $f = R_*\Omega_*/\sqrt{GM_*/R_*} = 5 \times 10^{-3}$), the fast magneto-acoustic surface is very close to the Alfvén surface in the fast-wind regimes. Close to the equator, the two surface are distinct, and the fast magneto-acoustic surface extends further away than the Alfvén surface. Figure 6 shows the extent of the fast magneto-acoustic surface in all of our simulations (hereafter referred to as the fast Alfvén surface/radius). It is defined as the point where the squared fast Alfvén Mach number is unity:

$$M_{A,f}^2 = \frac{2v^2}{c_s^2 + v_A^2 + \sqrt{(c_s^2 + v_A^2)^2 - 4c_s^2v_{A,p}^2}} = 1, \quad (12)$$

where c_s is the sound speed, v_A the Alfvén speed, and $v_{A,p}$ the poloidal Alfvén speed (without the φ component). As already shown by this contour in Figure 3, the location of the fast Alfvén radius is variable with latitude and oscillates between a maximum value at the pole and minimum value close to the equator, at the boundary between the slow- and fast-wind components. The interval between these two values is represented in Figure 6 with colored shades, each color being associated with a value of λ_* . For low values of δv_* , the fast Alfvén surface can extend to very large distances, up to $90R_*$.

The averaged fast Alfvén radii are reported in Table 2. The fast Alfvén radius is a decreasing function of the input energy

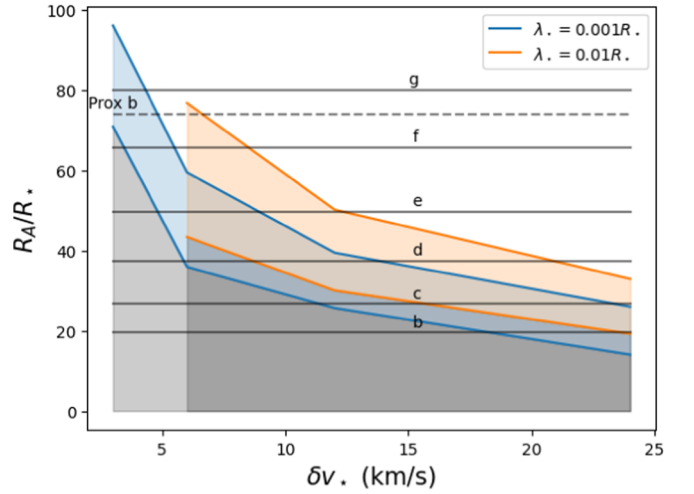


Figure 6. Extent of the fast Alfvén surface as a function of δv_* . Gray regions mark the minimum value of the fast Alfvén surface. Colored shades show its latitudinal variability for both values of λ_* . Horizontal black lines represent the semimajor axis of the first six planets of the TRAPPIST-1 system. For all simulations, at least one planet is within the maximal fast Alfvén radius, and can thus give birth to star–planet interactions. The dashed black line is the semimajor axis of Proxima Cen b in stellar radii.

and δv_* . This is a natural consequence of the increasing mass-loss rate with increasing δv_* . In Equation (12), the mass-loss rate is at the numerator, and increasing either the wind speed or the mass density will make the wind cross the fast Alfvénic surface closer to the star. Moreover, it only depends weakly on the turbulence correlation length scale. This is due to the fact that the mass-loss rate itself does not depend too much on λ_* (see Figure 5). Most of the effect of λ_* on the wind speed occurs beyond the sonic point (located at $\sim 2R_*$ in the fast-wind regime of our simulations), and as such the acceleration due to the wave pressure is done at constant mass flux, which conserves the location of the fast Alfvén point.

The semimajor axis of the orbit of the six first planets of the TRAPPIST-1 system are also represented in Figure 6. Looking at the range $\delta v_* = 3\text{--}12 \text{ km s}^{-1}$, which is the most consistent with the expected mass-loss rate obtained through Wood’s law, we observe that at least planet b must lie within the Alfvén surface. The maximum and minimum of the fast Alfvén surface can also be interpreted as a proxy for the inclination of the stellar dipole with respect to the ecliptic plane. The most favorable case corresponds to one wherein the dipole axis is contained in the ecliptic plane. The most unfavorable case is one wherein the dipole axis has a slight inclination that corresponds precisely to the minimum of the fast Alfvén surface, which appears unlikely. In the most favorable case ($\delta v_* = 3 \text{ km s}^{-1}$ and a strongly inclined dipole field), up to six planets are within the fast Alfvén zone for part of their orbit.

Hence, we can reasonably expect the TRAPPIST-1 system to be subject to several star–planet magnetic interactions, where the orbital motion of the planet excites waves that are able to come back to the host star, creating enhanced chromospheric emission (A. Strugarek et al. 2015; A. Strugarek 2016; A. Strugarek et al. 2019). Unfortunately, such interactions are very difficult to observe, and we do not know of any detection made for the TRAPPIST-1 system. However, our simulations are quite general and may apply to other systems. We now focus on a well-known system for which such detections have been claimed.

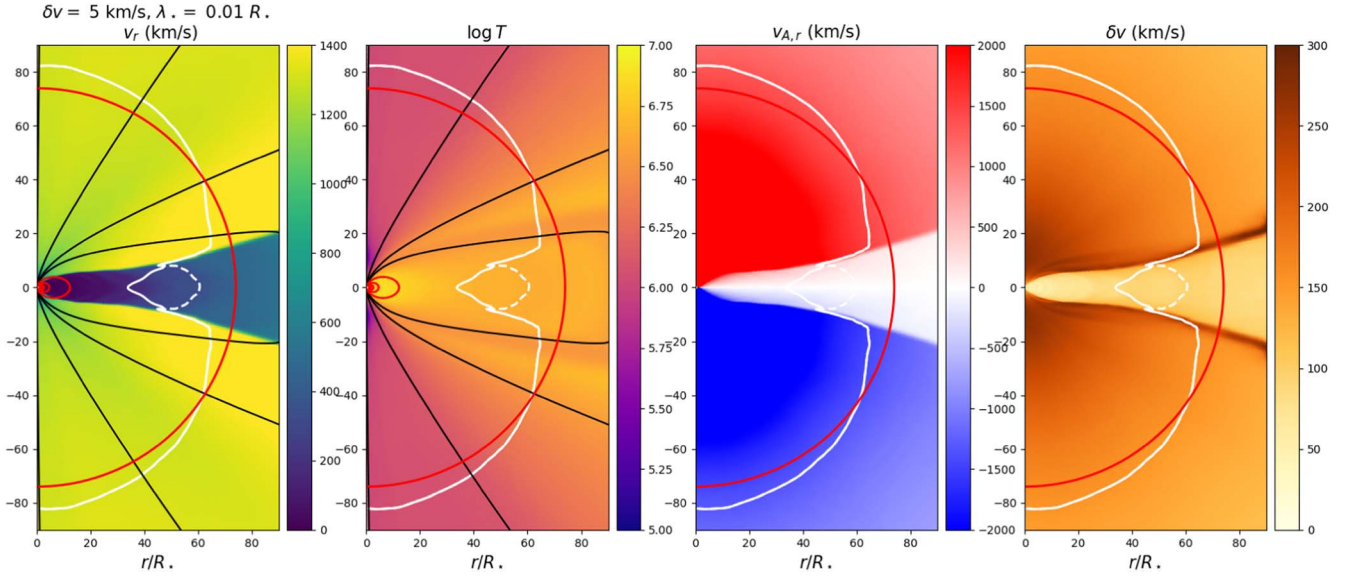


Figure 7. Same as Figure 3, for the Proxima Cen stellar parameters and $\delta v_* = 5 \text{ km s}^{-1}$ and $\lambda_* = 0.01 R_*$. The mass-loss rate of the simulation is at the upper bound $\dot{M} = 0.17 \dot{M}_\odot$. The semimajor axis of Proxima Cen b is shown in red, within or very close to the (fast) Alfvén surface of the stellar wind.

5.2. SPMI Detection for Proxima Cen b

The discovery of Proxima Cen b, a possible terrestrial planet, in the HZ of the closest star to the Sun (G. Anglada-Escudé et al. 2016), has triggered a renewed interest in the system. In particular, M. Pérez-Torres et al. (2021) detected a radio signal in the 1.1–3.1 GHz range, compatible with the electron cyclotron maser (ECM) emission that we observe for close-in star–planet or planet–satellite interactions (such as the Jupiter–Io system; see P. Zarka et al. 1996).

For these emissions to be effectively due to an ECM process, the planet, or at least part of its orbit, must lie within the fast Alfvén surface of the star. Proxima Cen is a M5.5V-type star of mass $M_* = 0.12 M_\odot$ and radius $R_* = 0.14 R_\odot$ (T. S. Boyajian et al. 2012). The escape velocity of Proxima Cen is $v_{\text{esc}} = 565 \text{ km s}^{-1}$, only slightly larger than the TRAPPIST-1 system (where $v_{\text{esc}} = 529 \text{ km s}^{-1}$). Hence, the normalization parameters are relatively close to the one used for the previous numerical study. Moreover, the magnetic flux has been estimated at $Bf = 600 \pm 150 \text{ G}$ (A. Reiners & G. Basri 2008; B. Klein et al. 2021), which is very similar to the amplitude measured for TRAPPIST-1. The rotation rate of the star is much smaller, with a period estimated at $P = 83$ days, and should play an even smaller role in the stellar wind dynamics than for TRAPPIST-1. It is thus reasonable to assume that the previous parameter study also applies to Proxima Cen.

Observations of the quiescent X-ray flux of Proxima Cen fall between 4 and $16 \times 10^{26} \text{ erg s}^{-1}$ (B. M. Haisch et al. 1990; B. Fuhrmeister et al. 2022). Assuming an average value $F_X = 10^{27} \text{ erg s}^{-1}$, the expected mass-loss rate through Wood’s law is

$$\begin{aligned} \dot{M}_* &= 3.8 \times 10^{11} \text{ g s}^{-1} \\ &= 0.25 \dot{M}_\odot. \end{aligned} \quad (13)$$

An upper limit for the mass-loss rate has been derived moreover by B. E. Wood et al. (2001), due to nondetection. This upper limit is $\dot{M}_* = 2.5 \times 10^{11} \text{ g s}^{-1}$ or $\dot{M}_* = 0.17 \dot{M}_\odot$, with the value used throughout this paper, $\dot{M}_\odot = 1.5 \times 10^{12} \text{ g s}^{-1}$.

Given these constraints on the mass-loss rate, and referring to Figure 5, we see that simulations with an input parameter $\delta v_* = 3\text{--}6 \text{ km s}^{-1}$ could well characterize the Proxima Cen wind. In Figure 6, we plot in dashed black the semimajor axis of the planet b, for which star–planet interactions have been detected. We see that this interval of δv_* is fully consistent with a planet orbiting within or very close to the fast Alfvén surface, which could explain these observations.

For completeness, we perform one simulation with $\delta v_* = 5 \text{ km s}^{-1}$, $\lambda_* = 0.01 R_*$, and the stellar parameters of Proxima Cen. Figure 7 shows the quasi-steady solution in the fashion of Figure 3. The parameters of the simulation have been chosen so that the mass-loss rate is

$$\begin{aligned} \dot{M}_* &= 2.55 \times 10^{11} \text{ g s}^{-1}, \\ &= 0.17 \dot{M}_\odot, \end{aligned} \quad (14)$$

precisely at the upper limit given by B. E. Wood et al. (2001). The orbit of the planet is below the maximum of the fast Alfvén surface, and remains close even for a weak inclination of the stellar dipole. It thus could be at the origin of the radio signal detected by M. Pérez-Torres et al. (2021). Note that with a lower mass-loss rate, the fast Alfvén surface would extend further, encompassing more of the orbit of Proxima Cen b.

6. X-Ray and UV Emissions

The final section of this paper is dedicated to the soft X-ray, EUV and far-UV (FUV) emissions (0.5–180 nm) modeling for M-dwarf stellar corona. These emissions are of primary importance in assessing the chemistry of planetary atmospheres and their expected lifetimes due to atmospheric mass loss (see, e.g., J. Sanz-Forcada et al. 2011; J. M. Chadney et al. 2015). They are however very difficult to observe in their entirety due to absorption processes in the interstellar medium and must rely on models constrained at a few wavelengths.

In the following, we compare two techniques developed in recent years and compare them with observations and our simulations. We first rely on the technique introduced by S. Toriumi & V. S. Airapetian (2022) and S. Toriumi et al. (2022) and

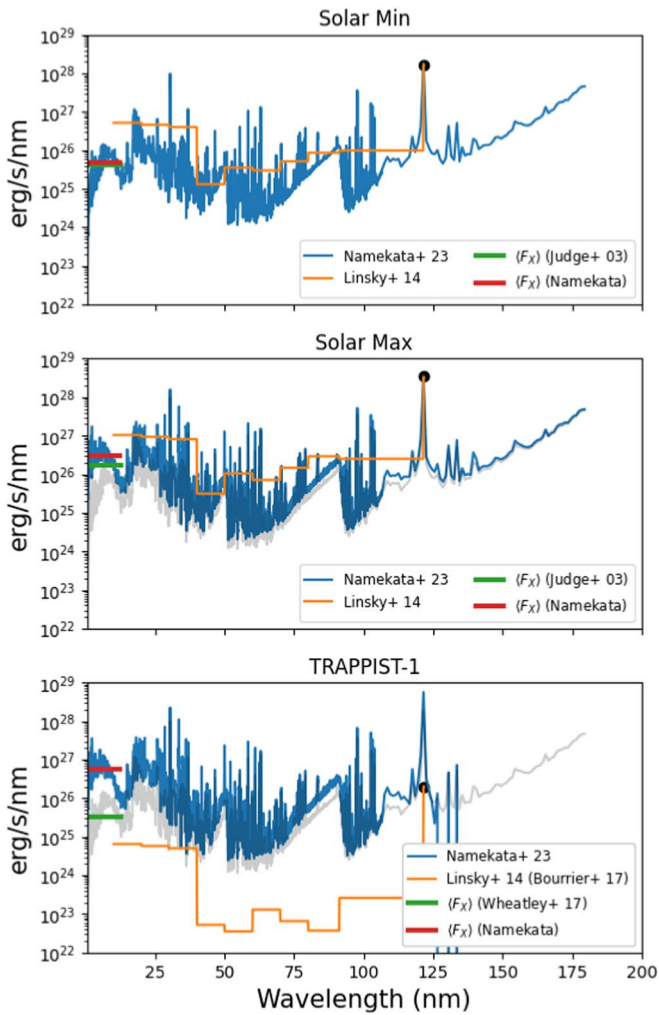


Figure 8. Reconstructed spectrum (0.5–180 nm) of the Sun (minimum and maximum) and TRAPPIST-1 using the F - Φ scaling relation of K. Namekata et al. (2023, blue), and the $F(\text{EUV})$ - $F(\text{Ly}\alpha)$ of J. L. Linsky et al. (2014, orange). The peak of the $\text{Ly}\alpha$ line is used to constrain the J. L. Linsky et al. (2014) extrapolation. It is taken from V. Bourrier et al. (2017b) in the case of TRAPPIST-1. The observed X-ray flux is shown in green, while the average value from the K. Namekata et al. (2023) extrapolation is shown in red. The gray shaded spectrum in the middle and bottom panels is the observed solar minimum spectrum of the top panel.

further developed by K. Namekata et al. (2023), which derives a scaling relationship between the X-ray and UV spectra of the Sun and the observed unsigned magnetic flux:

$$I(\nu) = I_0(\nu) + 10^{\beta(\nu)}(\Phi - \Phi_0)^{\alpha(\nu)}, \quad (15)$$

where the intensity I_0 is the spectral intensity at solar minimum, ν the wavelength, and $\Phi_0 = 1.18 \times 10^{23}$ Mx the unsigned magnetic flux at solar minimum. A machine-readable table of values for $I_0(\nu)$, $\alpha(\nu)$, and $\beta(\nu)$ is given in K. Namekata et al. (2023).

For TRAPPIST-1, we can get a rough estimate of the unsigned magnetic flux using the average value of the field, $\Phi_{\text{TRAP}} = 5.3 \times 10^{23}$ Mx. Figure 8 shows in blue the spectra at solar minimum (I_0), solar maximum (computed with $\Phi = 3.5 \times 10^{23}$ Mx), and for the TRAPPIST-1 system (note that with this technique, the estimated spectra of TRAPPIST-1 and Proxima Cen are identical). The solar blackbody radiation has been removed for TRAPPIST-1, which makes the UV spectrum vanish soon after the $\text{Ly}\alpha$ line at 121.5 nm.

We now compare these spectra with the method developed in J. L. Linsky et al. (2014). This work gives the average UV flux on the interval 10–117 nm, split in nine wavelength bands, based on the flux in the $\text{Ly}\alpha$ line. Figure 8 shows this extrapolation in orange, with $\text{Ly}\alpha$ fluxes taken from J. L. Linsky et al. (2014) for the Sun and V. Bourrier et al. (2017b) for TRAPPIST-1. X-ray fluxes in the range 0.1–2.4 keV are also shown for comparison, with values from P. G. Judge et al. (2003) for the Sun and P. J. Wheatley et al. (2017) for TRAPPIST-1.

Given the values of the unsigned magnetic flux used for the Sun and TRAPPIST-1 in the K. Namekata et al. (2023) estimates, the extrapolated spectra are quite close. In the case of the Sun, the formula of J. L. Linsky et al. (2014) is consistent with the magnetic flux formulation. For TRAPPIST-1, however, we obtain a much smaller UV irradiation. While the unsigned magnetic flux of the Sun and TRAPPIST-1 are close, the $\text{Ly}\alpha$ luminosity differs by 2 orders of magnitude. V. Bourrier et al. (2017a, 2017b) measured the total $\text{Ly}\alpha$ luminosity of TRAPPIST-1 around 2×10^{26} erg s $^{-1}$, while solar values range between 1.5 and 3.5×10^{28} erg s $^{-1}$. Hence, depending on the observable used for the calibration and extrapolation, unsigned magnetic flux or $\text{Ly}\alpha$ luminosity, we obtain two very different UV spectra. Interestingly, the X-ray flux of the Sun and TRAPPIST-1 are quite close, and while the UV spectra lie above the X-ray in the solar case, the opposite is observed for TRAPPIST-1 using J. L. Linsky et al. (2014). This suggests that the chromosphere and TR of very late M-type stars, from which most of the $\text{Ly}\alpha$ emission is coming from, behave differently to solar-like stars.

Direct modeling of the stellar spectra has been performed for TRAPPIST-1 (S. Peacock et al. 2019a) and other M-type stars (S. Peacock et al. 2019b). The authors used 1D models of the stellar atmosphere considering a fine resolution of the TR. A similar approach is not adequate with multi-dimensional (multi-D) models where the TR resolution is rarely sufficient. As explained in Section 3, a numerical technique is used to broaden the TR, which makes the reconstructed spectra (with CHIANTI, for example) unrealistic, especially in the $\text{Ly}\alpha$, which makes up for most of the radiated energy in the FUV. Nevertheless, our treatment of the TR guarantees that the integrated radiative losses and heating are equivalent to the fully resolved TR, and we can thus precisely constrain the energy budget of the simulations. From the extrapolations of Figure 8, we can compute the integrated losses in the UV range 10–121.7 nm, and compare it to the value obtained in our simulations. For both models the $\text{Ly}\alpha$ makes up for 60%–70% of the integral. Note that we discarded the soft X-ray range, mostly due to small-scale magnetic structure, which is not modeled in this study. While it is small compared to the $\text{Ly}\alpha$ line intensity for the Sun, it could be significant for TRAPPIST-1 (see Figure 8). Figure 9 compares the total integrated radiated emission through the term L_{rad} , with the integrated spectrum of both models (10–121.7 nm). The red box identifies the simulation parameter range compatible with Wood’s law’s mass-loss rate. With the “Sun-as-a-star” approach of K. Namekata et al. (2023), the matching value for δv_* is around 6–12 km s $^{-1}$ depending on λ_* , which is consistent with our previous analysis. The value obtained with the J. L. Linsky et al. (2014) method is much lower, due to the observed $\text{Ly}\alpha$ luminosity of V. Bourrier et al. (2017b). Nevertheless, the integrated losses of our simulation, for the

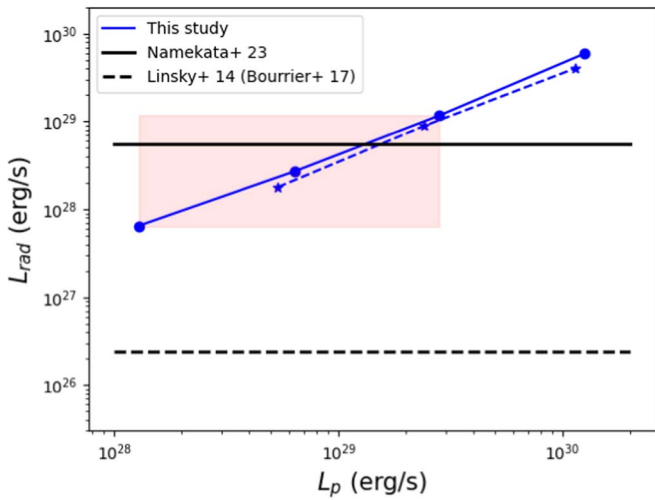


Figure 9. Radiative losses (same as Figure 5), compared with the integral of the TRAPPIST-1 synthetic spectrum in the EUV–FUV range (10–121.7 nm) with the method of K. Namekata et al. (2023) and J. L. Linsky et al. (2014). Plain and dashed blue lines correspond to $\lambda_* = 0.001R_\odot$ and $\lambda_* = 0.01R_\odot$, respectively. The red box identifies the parameter range compatible with Wood’s law’s mass-loss rate.

lowest value of the input Poynting flux, are in between these two estimates. Note that the dashed line estimate is a likely a lower bound of the integrated spectrum, as we observe the soft X-ray part of the TRAPPIST-1 spectrum to be more solar-like. Future works shall attempt to bridge the gap between simulations and observations in multiple lines of the X-ray and UV spectra.

7. Summary

M-dwarf stellar winds and stellar environments have been subject to a great amount of attention in the context of the search for habitable planets. As for most stellar winds, observations are scarce, and scenarios of magnetospheric or atmospheric interaction with the host star must rely on models. In this work, we propose a strategy based on the latest measurements of mass-loss rate detected through Ly α absorption at the astropause (B. E. Wood et al. 2021). We define an acceptable mass-loss rate region between one-tenth and 10 times the fitted law of B. E. Wood et al. (2021) that any simulation should aim for varying its input parameters. It is indeed impossible at the moment to constrain from first physical principles the input energy that is transferred from the photosphere of a given star to its corona and stellar wind. Moreover, input parameters depend on the model and the coronal heating and wind acceleration mechanisms chosen.

We rely here on the Alfvén-wave-driven scenario, using the multi-D WindPredict-AW code. We perform nine simulations varying the input parameters δv_* and λ_* . We show through a global energy balance, expressed in unit of ergs per second (or luminosity; see T. K. Suzuki et al. 2013; M. Shoda & S. Takasao 2021, for similar approaches), that the input energy is distributed between radiative losses and kinetic energy transferred to the wind. Throughout our parameter scan, radiative losses always strongly dominate the kinetic energy balance, and we wish to strongly underline that special care should be brought to the treatment of the TR. In multi-D simulations, the TR has to be broadened to limit numerical cost. We use a cutoff temperature technique, inspired by R. Lionello et al. (2009) and refined by C. D. Johnston et al. (2020), to adapt the TR to our numerical resolution and ensure that

the radiative losses and heating are equivalent to a fully resolved TR.

Our study then shows that the stellar wind properties do depend on the wind acceleration model and the input parameters. In particular, while the initial velocity perturbation δv_* controls the amplitude of the input Poynting flux, we highlight the influence of the turbulence correlation length scale on the terminal wind speed obtained in the simulations. This parameter, λ_* , controls the height of the energy deposition by Alfvén-wave turbulence in the corona and stellar wind. In the range of acceptable mass-loss rates, we have been able to run simulations with $\lambda_* = 0.001R_*$ and $\lambda_* = 0.01R_*$. The highest value gives birth, for the same input energy, to higher wind speeds than the fast solar wind, up to 1200 km s^{-1} . The turbulence correlation length scale is usually related to the average size of granules or supergranules emerging at the top of the convective envelope, and the typical value used in solar-like simulations is $\lambda_\odot = 0.01R_\odot$ (supergranule size; see B. van der Holst et al. 2014; V. Réville et al. 2020). Some works have claimed however that this value should be closer to the size of granules $0.001R_\odot$ (A. A. van Ballegoijen & M. Asgari-Targhi 2017). M dwarfs have deep convection zones, and can be fully convective. Differences in the small-scale organization of the magnetic field of M dwarfs could lead to either one or the other parameter choice. Note also that the size of the convective structure might be uncorrelated from the size of the star. That being said, the actual function of the turbulent length scale in the simulations is to control the height of the turbulent dissipation, which needs to heat sufficiently the low corona to create enough thermal and dynamic pressure to open the very intense dipolar magnetic field and sustain a $\sim 10^6 \text{ K}$ corona. This may be achieved differently depending on the coronal heating model.

In the case of TRAPPIST-1, we thus give possible values of the stellar wind speed and mass-loss rate compatible with Wood’s law. We find that for this range of parameters, 2–6 planets are orbiting within the fast Alfvén surface of the stellar wind. This suggests that strong star–planet magnetic interactions are at play in this system. For planets e and f, which lie in the usual HZ (see M. Turbet et al. 2020, for a review of atmospheric processes), such processes may be considered. Previous works studying TRAPPIST-1 have found different and contradictory results. It is unclear why these previous studies’ results are different, but our results are consistent with detection of radio emission in Proxima Cen (M. Pérez-Torres et al. 2021).

Our parameter study can indeed be applied to this nearby system, and we found that Proxima Cen b is also likely to orbit within the fast Alfvén surface. Our conclusions thus differ from the one of R. D. Kavanagh et al. (2021). The latter work used the Zeeman Doppler imaging (ZDI) observations of B. Klein et al. (2021), which obtain a large-scale field strength of $\sim 200 \text{ G}$, significantly smaller than the unsigned flux amplitude of A. Reiners & G. Basri (2008). Whether stellar wind simulations should use one or the other can be discussed (see S. Hazra et al. 2021, for a study of these effects along the solar cycle). Using a dipole of 600 G, we account for all the detected magnetic flux, even if part of it is concentrated at small scales and may be absent from ZDI reconstructions. We thus consider a maximal case in terms of magnetic field amplitude. The differences may be also explained by the fact that they have obtained a mass-loss rate that is above the nondetection limit of B. E. Wood et al. (2021), if only slightly, and that they have




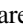
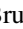


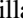

considered only the Alfvén surface. Our results thus call for a reevaluation of the environment of Proxima Cen b (see L. Peña-Moñino et al. 2024).

Finally, we attempt to use reconstructed X-ray and UV spectra to constrain our simulations. We use two different approaches that lead to very different results. The first approach is to scale the solar X-ray and UV emissions to the total unsigned magnetic flux of a given star (K. Namekata et al. 2023). Using this approach, we find a spectrum for TRAPPIST-1 similar to the Sun during its maximum of activity. The integrated losses in the EUV–FUV band (10–121.7 nm) are consistent with the radiation losses obtained in our simulations, for the right mass-loss rate range. However, the peak of the Ly α line is much higher than observed by V. Bourrier et al. (2017a). The second reconstruction, based on J. L. Linsky et al. (2014) and calibrated by the observed peak in Ly α , yields thus a much lower UV flux from TRAPPIST-1 than what is predicted by the unsigned flux approach and our simulations. None of these reconstructions have been intended for very low mass stars, the study of J. L. Linsky et al. (2014) going down to M5 stars. Our simulations are moreover certainly closer to the “Sun-as-a-star” approach of K. Namekata et al. (2023), which explains the better agreement. This discrepancy appears as an interesting friction point that should be addressed in further studies, through for example a special attention to the TR where most of the Ly α emission is coming from.

Acknowledgments

We thank the referee for insightful comments that significantly improved the manuscript. V.R. thanks Miguel Pérez-Torres, Vincent Bourrier, Jean-François Donati, Claire Moutou, Chen Shi, and Susanna Parenti for useful discussions. J.M.J., M.V., and N.M. acknowledge support from the Jet Propulsion Laboratory, California Institute of Technology, under a contract with NASA. V.R., J.M.J., M.V., N.M., and L.H.R. acknowledge support of the NASA-ROSES Exoplanet Research Program (grant No. 80NM0018F0610). Simulations were performed on the IDRIS/Irene supercomputer through the GENCI grant A0150410293. A.S. acknowledges funding from the Programme National de Planétologie (INSU/PNP), a PLATO/CNES grant at CEA/IRFU/DAP, the DIM-ACAV+ ANAIS2 project, the ERC EXOMAGNETS consolidator grant No. 101125367, the DIM/Origines DynamEarth project, and the MERAC foundation. A.S.B. acknowledges support from the Programme National Soleil Terre (PNST) and the ERC WholeSun #810218. The authors are grateful to the PLUTO development team. CHIANTI is a collaborative project involving George Mason University, the University of Michigan (USA), University of Cambridge (UK), and NASA Goddard Space Flight Center (USA).

ORCID iDs

Victor Réville  <https://orcid.org/0000-0002-2916-3837>
 Jamie M. Jasinski  <https://orcid.org/0000-0001-9969-2884>
 Marco Velli  <https://orcid.org/0000-0002-2381-3106>
 Antoine Strugarek  <https://orcid.org/0000-0002-9630-6463>
 Allan Sacha Brun  <https://orcid.org/0000-0002-1729-8267>
 Neil Murphy  <https://orcid.org/0000-0001-6102-7563>
 Leonardo H. Regoli  <https://orcid.org/0000-0002-7628-1510>
 Alexis P. Rouillard  <https://orcid.org/0000-0003-4039-5767>
 Jacobo Varela  <https://orcid.org/0000-0002-6114-0539>

References

- Anglada-Escudé, G., Amado, P. J., Barnes, J., et al. 2016, *Natur*, 536, 437
 Bourrier, V., de Wit, J., Bolmont, E., et al. 2017a, *AJ*, 154, 121
 Bourrier, V., Ehrenreich, D., Wheatley, P. J., et al. 2017b, *A&A*, 599, L3
 Boyajian, T. S., von Braun, K., van Belle, G., et al. 2012, *ApJ*, 757, 112
 Chadney, J. M., Galand, M., Unruh, Y. C., Koskinen, T. T., & Sanz-Forcada, J. 2015, *Icar*, 250, 357
 Del Zanna, G., Dere, K. P., Young, P. R., & Landi, E. 2021, *ApJ*, 909, 38
 Dere, K. P., Landi, E., Mason, H. E., Monsignor Fossi, B. C., & Young, P. R. 1997, *A&AS*, 125, 149
 Dong, C., Jin, M., Lingam, M., et al. 2018, *PNAS*, 115, 260
 Finley, A. J., & Matt, S. P. 2017, *ApJ*, 845, 46
 Finley, A. J., & Matt, S. P. 2018, *ApJ*, 854, 78
 Fuhrmeister, B., Zisik, A., Schneider, P. C., et al. 2022, *A&A*, 663, A119
 Garraffo, C., Drake, J. J., & Cohen, O. 2016, *ApJL*, 833, L4
 Garraffo, C., Drake, J. J., Cohen, O., Alvarado-Gómez, J. D., & Moschou, S. P. 2017, *ApJL*, 843, L33
 Gillon, M., Jehin, E., Lederer, S. M., et al. 2016, *Natur*, 533, 221
 Gillon, M., Triaud, A. H. M. J., Demory, B.-O., et al. 2017, *Natur*, 542, 456
 Güdel, M. 2004, *A&ARv*, 12, 71
 Haisch, B. M., Butler, C. J., Foing, B., Rodono, M., & Giampapa, M. S. 1990, *A&A*, 232, 387
 Hazra, S., Réville, V., Perri, B., et al. 2021, *ApJ*, 910, 90
 Hollweg, J. V. 1976, *JGR*, 81, 1649
 Jardine, M., & Collier Cameron, A. 2019, *MNRAS*, 482, 2853
 Johnston, C. D., Cargill, P. J., Hood, A. W., et al. 2020, *A&A*, 635, A168
 Judge, P. G., Solomon, S. C., & Ayres, T. R. 2003, *ApJ*, 593, 534
 Kavanagh, R. D., Vidotto, A. A., Klein, B., et al. 2021, *MNRAS*, 504, 1511
 Klein, B., Donati, J.-F., Hébrard, É. M., et al. 2021, *MNRAS*, 500, 1844
 Lecavelier Des Etangs, A. 2007, *A&A*, 461, 1185
 Lehmann, L. T., Donati, J.-F., Fouqué, P., et al. 2024, *MNRAS*, 527, 4330
 Linsky, J. L., Fontenla, J., & France, K. 2014, *ApJ*, 780, 61
 Lionello, R., Linker, J. A., & Mikić, Z. 2009, *ApJ*, 690, 902
 Luger, R., Sestovic, M., Kruse, E., et al. 2017, *NatAs*, 1, 0129
 Mignone, A., Bodo, G., Massaglia, S., et al. 2007, *ApJS*, 170, 228
 Morin, J., Donati, J.-F., Petit, P., et al. 2008, *MNRAS*, 390, 567
 Moutou, C., Hébrard, E. M., Morin, J., et al. 2017, *MNRAS*, 472, 4563
 Namekata, K., Toriumi, S., Airapetian, V. S., et al. 2023, *ApJ*, 945, 147
 Parenti, S., Réville, V., Brun, A. S., et al. 2022, *ApJ*, 929, 75
 Parker, E. N. 1988, *ApJ*, 330, 474
 Peacock, S., Barman, T., Shkolnik, E. L., Hauschildt, P. H., & Baron, E. 2019a, *ApJ*, 871, 235
 Peacock, S., Barman, T., Shkolnik, E. L., et al. 2019b, *ApJ*, 886, 77
 Peña-Moñino, L., Pérez-Torres, M., Varela, J., & Zarka, P. 2024, *A&A*, 688, A138
 Pérez-Torres, M., Gómez, J. F., Ortiz, J. L., et al. 2021, *A&A*, 645, A77
 Reiners, A., & Basri, G. 2008, *A&A*, 489, L45
 Reiners, A., & Basri, G. 2010, *ApJ*, 710, 924
 Reiners, A., Shulyak, D., Käpylä, P. J., et al. 2022, *A&A*, 662, A41
 Réville, V., Brun, A. S., Matt, S. P., Strugarek, A., & Pinto, R. F. 2015, *ApJ*, 798, 116
 Réville, V., Fargette, N., Rouillard, A. P., et al. 2022, *A&A*, 659, A110
 Réville, V., Parenti, S., Brun, A. S., et al. 2021, in SF2A-2021: Proc. the Annual meeting of the French Society of Astronomy and Astrophysics (Besançon, France, 2021) ed. A. Siebert et al., 230
 Réville, V., Velli, M., Panasenco, O., et al. 2020, *ApJS*, 246, 24
 Sanz-Forcada, J., Micela, G., Ribas, I., et al. 2011, *A&A*, 532, A6
 Schmelz, J. T., Reames, D. V., von Steiger, R., & Basu, S. 2012, *ApJ*, 755, 33
 Shi, C., Velli, M., Lionello, R., et al. 2023, *ApJ*, 944, 82
 Shoda, M., & Takasao, S. 2021, *A&A*, 656, A111
 Strugarek, A. 2016, *ApJ*, 833, 140
 Strugarek, A., Brun, A. S., Donati, J. F., Moutou, C., & Réville, V. 2019, *ApJ*, 881, 136
 Strugarek, A., Brun, A. S., Matt, S. P., & Réville, V. 2014, *ApJ*, 795, 86
 Strugarek, A., Brun, A. S., Matt, S. P., & Réville, V. 2015, *ApJ*, 815, 111
 Strugarek, A., Fares, R., Bourrier, V., et al. 2022, *MNRAS*, 512, 4556
 Suzuki, T. K., Imada, S., Kataoka, R., et al. 2013, *PASJ*, 65, 98
 Toriumi, S., & Airapetian, V. S. 2022, *ApJ*, 927, 179
 Toriumi, S., Airapetian, V. S., Namekata, K., & Notsu, Y. 2022, *ApJS*, 262, 46
 Turbet, M., Bolmont, E., Bourrier, V., et al. 2020, *SSRv*, 216, 100
 van Ballegoijen, A. A., & Asgari-Targhi, M. 2017, *ApJ*, 835, 10
 van der Holst, B., Sokolov, I. V., Meng, X., et al. 2014, *ApJ*, 782, 81
 Van Grootel, V., Fernandes, C. S., Gillon, M., et al. 2018, *ApJ*, 853, 30
 Varela, J., Brun, A. S., Strugarek, A., et al. 2022a, *A&A*, 659, A10

- Varela, J., Brun, A. S., Zarka, P., et al. 2022b, *SpWea*, **20**, e2022SW003164
- Velli, M. 1993, *A&A*, **270**, 304
- Velli, M. 2010, in *AIP Conf. Ser.* 1216, Twelfth Int. Solar Wind Conf., ed. M. Maksimovic et al. (Melville, NY: AIP), 14
- Wheatley, P. J., Louden, T., Bourrier, V., Ehrenreich, D., & Gillon, M. 2017, *MNRAS*, **465**, L74
- Wood, B. E., Linsky, J. L., Müller, H.-R., & Zank, G. P. 2001, *ApJL*, **547**, L49
- Wood, B. E., Müller, H.-R., Redfield, S., et al. 2021, *ApJ*, **915**, 37
- Wood, B. E., Müller, H.-R., Zank, G. P., Linsky, J. L., & Redfield, S. 2005, *ApJL*, **628**, L143
- Zarka, P., Farges, T., Ryabov, B. P., Abada-Simon, M., & Denis, L. 1996, *GeoRL*, **23**, 125